Few Layer $MnPS_3$

February 20, 2023 · salve-project.de/newspress/few-layer-mnps3.html

February 20, 2023 – Manganese phosphorus trisulfide ($MnPS_3$) is a particularly interesting material in the context of magnetism in a system with reduced dimensionality. A team of researchers from Ulm University and the Helmholtz-Zentrum Dresden-Rossendorf in Germany has presented an experimental and theoretical study on modifying the properties of free-standing quasi-two-dimensional (2D) $MnPS_3$ by local structural transformations via electron irradiation and thermal annealing, which may open opportunities to build new devices for the storage of quantum information.

Material design is an attractive idea that is very difficult to implement in practice. Combining the best of different ingredients to create the ultimate material is a task[1] that calls for a tool able to change the structure of a material at the atomic level[2]. The ability to characterize and change materials atom by atom is as important for progress in nanotechnology[3],[4] as precise control over their growth. Aberration-corrected (AC) high-resolution (HR) in situ transmission electron microscopy (TEM)[5],[6], along with scanning transmission electron microscopy (STEM)[7], has proven especially useful here, because it delivers information about the atomic rearrangement in a sample under electron irradiation in real time[2],[8]. Depending on the chosen electron beam size, (S)TEM techniques can make structural changes locally, down to the atomic level[9], as a result of the interaction of the highly accelerated electrons with the sample[10],[11].

The modification of ultrathin nanosheets has recently attracted considerable attention, because the structure, and thus the properties, of two-dimensional (2D) materials can be altered more easily than in bulk systems owing to their geometry. In particular, the crystallographic, electronic and magnetic properties of 2D materials[12] can be tuned by creating single[13] and extended defects[14]–[16] and by adsorbing atoms[17]. In addition, (S)TEM can be used to drive spatially confined phase transformations in crystalline materials with few layers or monolayers, thereby significantly changing their local properties. Controllable structural transformations have been reported in transition metal dichalcogenides (TMDs)[13],[18]–[20], alumina[21], silica[21] and nanowires[22],[23]. The advantage of electron-beam-mediated modification over conventional methods such as heating[24], electrostatic gating[25] or strain engineering[26] is the real-time control of the transformation process down to the atomic scale[19],[22]. (S)TEM is thus an excellent tool for locally controlling the properties of 2D materials.

Within the class of 2D materials, the transition metal phosphorus trisulfides (TMPTs) have recently come into the focus of researchers, and manganese phosphorus trisulfide ($MnPS_3$) has received the most attention among them. It is a layered antiferromagnet with a wide band gap whose properties can be manipulated in many ways; its structure and the routes to tune it are summarized in the first box.

$MnPS_3$: a magnetic layered host and its tunability

$MnPS_3$ crystallizes in the monoclinic space group C2/m[27]. The magnetic Mn^{2+} ions are coordinated octahedrally by six S atoms, and dumbbell-shaped $[P_2S_6]^{4-}$ units with P–P pairs occupy the centres of the Mn hexagons[28]. The side and top views of the structure, the unit cell and the projection along the normal incidence direction [103] are shown in Fig. 1, together with an 80-kV HRTEM image of a few-layer flake viewed along that direction.

The material has inherent magnetic properties[29] that persist even when it is thinned down to a few layers[30], and a band gap of about 3 eV[31], which makes it a candidate for multifunctional electronics and spintronics[32] and for battery applications[33]. These intrinsic properties can be manipulated substantially: pressure-controlled compression alters the magnetic properties and forces an insulator-to-metal transition[34],[35], and suitable intercalation reduces the intralayer coupling and changes the magnetism[36],[37].

MnS-type systems, the end product of the transformations described below, are promising in their own right: α-MnS has been proposed as an anode material for post-lithium batteries[38],[39] and is an interesting candidate for future electronic devices such as field-effect transistors[40].

The authors had found earlier that few-layer TMPTs lose predominantly sulfur through the interaction with the incident electrons, which in turn leads to strong changes in the original material[41]. In the new study they turned to the properties of the free-standing $MnPS_3$/MnS systems that emerge from electron-beam-induced phase transformations and from annealing, starting with what the beam does to the lattice.

Fig. 2(a1–a3) shows an image sequence of 80-kV Cc/Cs-corrected HRTEM of few-layer $MnPS_3$ under the electron beam at a constant dose rate of 0.5×10^6 $e^-/(s\ nm^2)$. Fig. 2(a1) shows the pristine material in the normal incidence direction [103] of $MnPS_3$, with an enlarged region on the right. After irradiation, changes in the material become evident, as Fig. 2(a2–a3) shows: islands with an altered structure grow continuously within the host matrix, and their area increases linearly with the accumulated dose (Fig. 2b). As the authors' previous study had shown, the primary removal of sulfur (S) and phosphorus (P) atoms by 80-keV electrons proceeds via direct electron–nucleus collisions[41]. This leads to an S deficiency in the exposed regions of $MnPS_3$ and can therefore drive the growth of new structures. Where in the stack the new phase forms is explained in the second box.

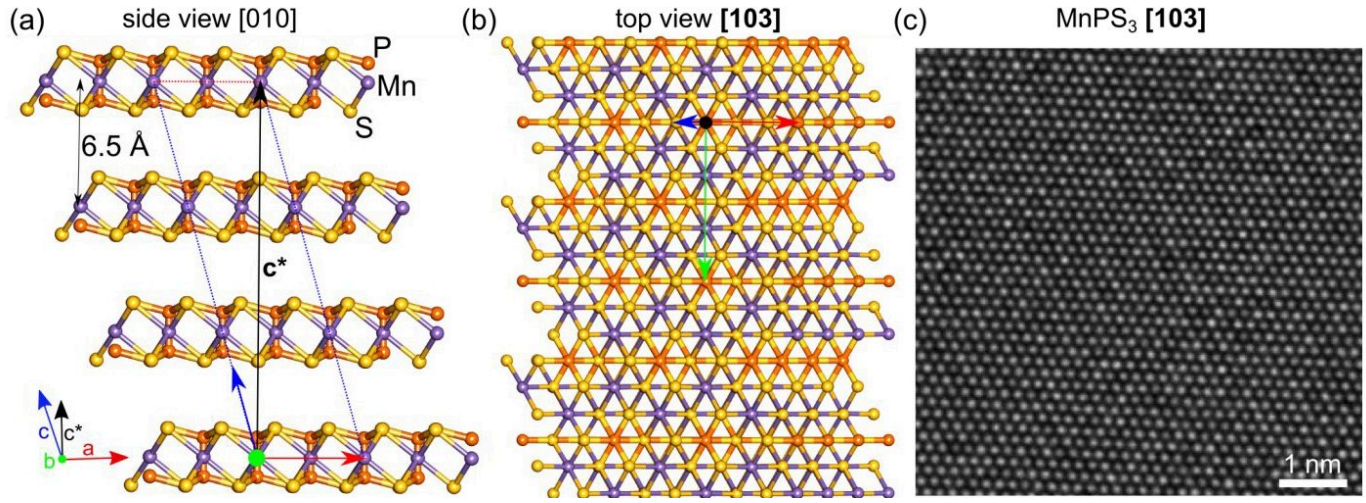

Fig. 1: Structural model of MnPS3

Layer by layer: where the new phase grows

Extensive studies (TEM experiments and calculations) on a wide variety of materials have shown that atoms in layers facing the electron beam are considerably less affected by sputtering through direct electron–nucleus collisions than those at the beam exit surface, here the bottom layer[41]. For a single layer in particular, the displacement thresholds for chalcogen atoms facing the beam (in the upper chalcogen layer) were found to be higher than for the lower chalcogen layer[8],[42]. If additional layers sit on top of a single layer, it can be assumed that the outer layers of the few-layer system are affected first, most likely the bottom layer (see the inset in Fig. 2b).

To illustrate the presumed transformation process in $MnPS_3$, an experimental image and two corresponding FFT-mask-filtered images are shown in Fig. 2c. When the $MnPS_3$ lattice is filtered with the FFT mask, that structure extends over the entire sample area, whereas the new structure is present only in the areas outlined in red. From this, the researchers concluded that the new phase spreads primarily laterally (in-plane), while intact $MnPS_3$ layers remain on top or underneath. A modelled bilayer scheme below the images visualizes the emerging structure (red) embedded in an isolated $MnPS_3$ layer (grey). While the first layer remains virtually intact, new structures emerge in the second layer through the removal of S and P atoms; the authors therefore proposed that the new structure grows within one layer after the other, starting at the bottom.

Three-dimensional electron diffraction (3D-ED) was used to determine the lattice parameters of the newly formed phases[43]. Few-layer $MnPS_3$ was irradiated until additional Bragg reflections of the new phases were clearly visible in the ED data (Fig. 3a,b). Two different new phases, labelled phase 1 and phase 2, appear; the reflections of phase 1 are more intense and correspond to the embedded phase seen in Fig. 2. The reconstructed diffraction volume[43] in Fig. 3c shows an overlay of two distinct crystalline lattices, the $MnPS_3$ host (blue) and the new phase 1 (red). Phase 1 turned out to be a cubic, NaCl-type lattice, closely related to the mineral alabandite, α-MnS, and oriented with its [111] direction along the [103] normal of the host; the authors assign it to α-$MnS_{1-x}P_x$ (Fig. 3d). Phase 2, which appears at later stages of the transformation, was identified as the hexagonal γ-$MnS_{1-x}P_x$ with a wurtzite structure[44]. The measured cell parameters and the reasoning behind the assignment are given in the third box.

3D electron diffraction: the unit cells of the new phases

The irradiated crystal was tilted in the TEM over a range of ±60° with a tilt step of 1°, a diffraction pattern was recorded at each tilt position, and the tilt series was reconstructed into a 3D reciprocal space (Fig. 3c). The extracted positions of the red reflections align well with a single lattice, which suggests that all inclusions have a similar orientation within the matrix. This new lattice is cubic with a = 2.47 Å, b = 2.56 Å, c = 2.67 Å, α = 90.1°, β = 89.4° and γ = 90.3°, and its lattice parameters correspond to the Mn–S bond length in $MnPS_3$ of 2.61 Å. Phase 1 is therefore a NaCl-type, F-centred lattice with a cell parameter of 5.21 Å. The most stable compound in the Mn–P–S system with this structure type is alabandite, α-MnS, with a lattice constant of 5.22 Å[45], space group Fm-3m and bivalent Mn. Because the composition of the new phase may deviate from strict MnS stoichiometry, it is assigned to α-$MnS_{1-x}P_x$. The peak at 1.84 Å in Fig. 3b can then be attributed to its 002 reflection, and the lattice is aligned with the [111] direction along the [103] reflection of the host, exactly the orientation seen in the HRTEM experiments of Fig. 2.

3D-ED cannot give the exact S:P ratio of the new phase or the Mn valence. A spatially resolved EELS analysis, however, showed that predominantly S is present and that Mn is predominantly 2+, so the combined experiments point to $Mn^{II,III}S_{1-x}P_x$ with the NaCl structure, a lattice parameter of 5.21 Å, a high S and a low P concentration.

The weak reflections of phase 2 appeared later, as small arcs and sometimes as parts of diffraction rings, which the authors attribute to a partial loss of its orientation relationship with the host. The search for a phase candidate yielded the hexagonal, wurtzite-type γ-$MnS_{1-x}P_x$[44]. Its characterization was complicated by the presence of the two other phases, but the reflection positions match the data well: the peak at 1.98 Å in Fig. 3b, for example, corre-

sponds to the 2-1-10 reflection of γ-$MnS_{1-x}P_x$, and ultrathin patches of phase 2 were also found in HRTEM images at a later transformation stage.

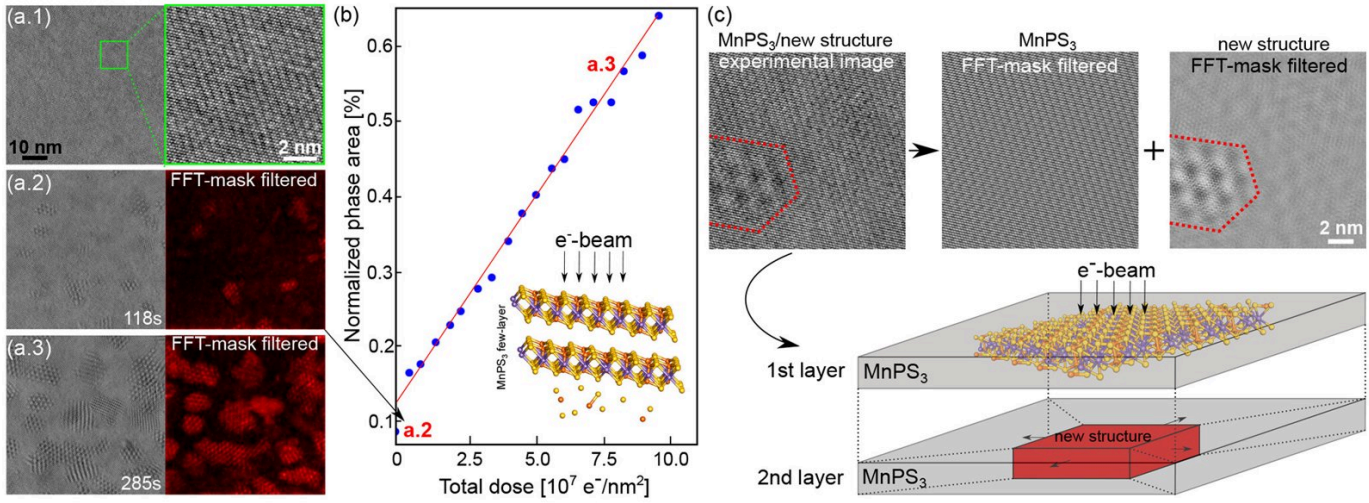

Fig. 2: Phase islands growing under the beam

The experiments thus indicate that at the beginning of the irradiation the electron beam transforms the host into cubic α-$MnS_{1-x}P_x$ oriented with its [111] direction parallel to the normal incidence [103] of the $MnPS_3$ matrix. With increasing imaging time, that is, a larger accumulated dose, free-standing patches of the newly formed phases could be imaged after the host material had completely degraded. Fig. 4a shows an experimental HRTEM image of a freshly grown, isolated α-$MnS_{1-x}P_x$ crystal, with a magnified section in the red frame; an overlay of the simulated image with the atomic model of the cubic phase along [111] highlights the atomic column contrast, and the lattice parameters agree with those found by 3D-ED (Fig. 3). At this stage, different orientations of α-$MnS_{1-x}P_x$ occur as free-standing structures as well: Fig. 4b shows a patch viewed along [001], with a magnified portion in the green outlined area, in good agreement with the simulated HRTEM image for this orientation. Fig. 4c shows a region of γ-$MnS_{1-x}P_x$ in the [0001] direction, magnified in blue, and again the observed contrast matches the corresponding image simulation.

Are such phosphorus-alloyed MnS phases stable at all? The energetics of the α- and γ-$MnS_{1-x}P_x$ phases formed at room temperature were studied with first-principles calculations, using the convex hull of the formation enthalpy, a standard approach in materials science to evaluate the relative stability of materials with different stoichiometries. The result, plotted in the right-hand panels of Fig. 4, is that several mixed compounds lie on or within a few meV of the hull, so that the mixing entropy stabilizes them at room temperature; the details are given in the fourth box.

Energetics of $MnS_{1-x}P_x$: convex hull, mixing entropy and the simulations behind the images

The convex hull was constructed from the formation enthalpy per atom, $H_{Form}(MnS_{1-x}P_x) = [E(MnS_{1-x}P_x) - x{\cdot}E(MnS) - (1-x){\cdot}E(MnP)]/2$, where x is the phosphorus concentration and the energies of the mixed compound and the pure phases come from DFT. For α-[111] $MnS_{1-x}P_x$, several mixed compounds (for example x = 0, 0.625 and 1) lie on the hull, which suggests that they are at least metastable. For the other compounds the energy differences to the hull are in the meV range, so that at room temperature the mixing entropy per atom, $S_{mix}(x) = -[x{\cdot}\ln(x) + (1-x){\cdot}\ln(1-x)]{\cdot}k_B/2$[46], can stabilize them; the Gibbs free energy difference $\Delta G = \Delta H - T{\cdot}S_{mix}$ to the hull is plotted on the right of Fig. 4. Compared with the [111] direction, $MnS_{1-x}P_x$ sheets with their surface along [001] are more stable over a wide range of low P concentrations, and in the γ phase the stabilization of the mixed compound along [0001] requires a higher fraction of phosphorus than in the α phase.

All calculations used spin-polarized density functional theory (VASP code) with the PBE exchange-correlation functional; electronic structures were computed with DFT+U (effective Hubbard U of 5.5 eV on Mn) and with the HSE06 hybrid functional. The stability analysis started from a relaxed 4 × 4 × 2 MnS supercell with a plane-wave cutoff of 400 eV and 2 × 2 × 1 k-points, in which S atoms were randomly replaced by P until MnP was reached; the configurational entropy was evaluated from the number of possible arrangements. The HRTEM image simulations in Fig. 4 were performed with the open-source multislice code abTEM, with the experimental imaging parameters as input, Poisson noise added for the finite dose and a stoichiometry of $MnS_{0.95}P_{0.05}$ assumed throughout.

Heat offers a second route to the same destination. Pristine $MnPS_3$ flakes of different thicknesses were heated in situ in steps of about 10 °C, and a structural transformation was observed at 490 °C. Afterwards the sample looked completely different: no large $MnPS_3$ flakes remained, but clustered polycrys-

talline nanocrystals had emerged, which indicates a complete structural transformation. To analyze the composition of a structure annealed at 600 °C, STEM HAADF images and EDX elemental maps were acquired at 80 kV from different sample positions (Fig. 5a); the maps of Mn and S prove the presence of these elements, and the EDX spectrum and quantification in Fig. 5b show mainly Mn and S, with small amounts of C, O and residual P. Core-loss EELS of the Mn $L_{2,3}$ edge (Fig. 5c) gave a white-line ratio[47] of L_3 to L_2 of 4.50, which indicates that the structure contains mainly Mn^{2+}[41],[47]. Electron diffraction of the annealed sample, azimuthally integrated in Fig. 5d, agrees well with a simulated powder pattern of alabandite, the face-centred cubic $Mn^{2+}S^{2-}$, and HRTEM confirmed it: a typical grain (Fig. 5e,f) shows a cubic lattice along [100] with atomic column distances of 2.60 and 2.58 Å, in good agreement with the expected 2.62 Å[45] for alabandite projected along [100]. Protocol, contaminants and the diffraction numbers are collected in the fifth box.

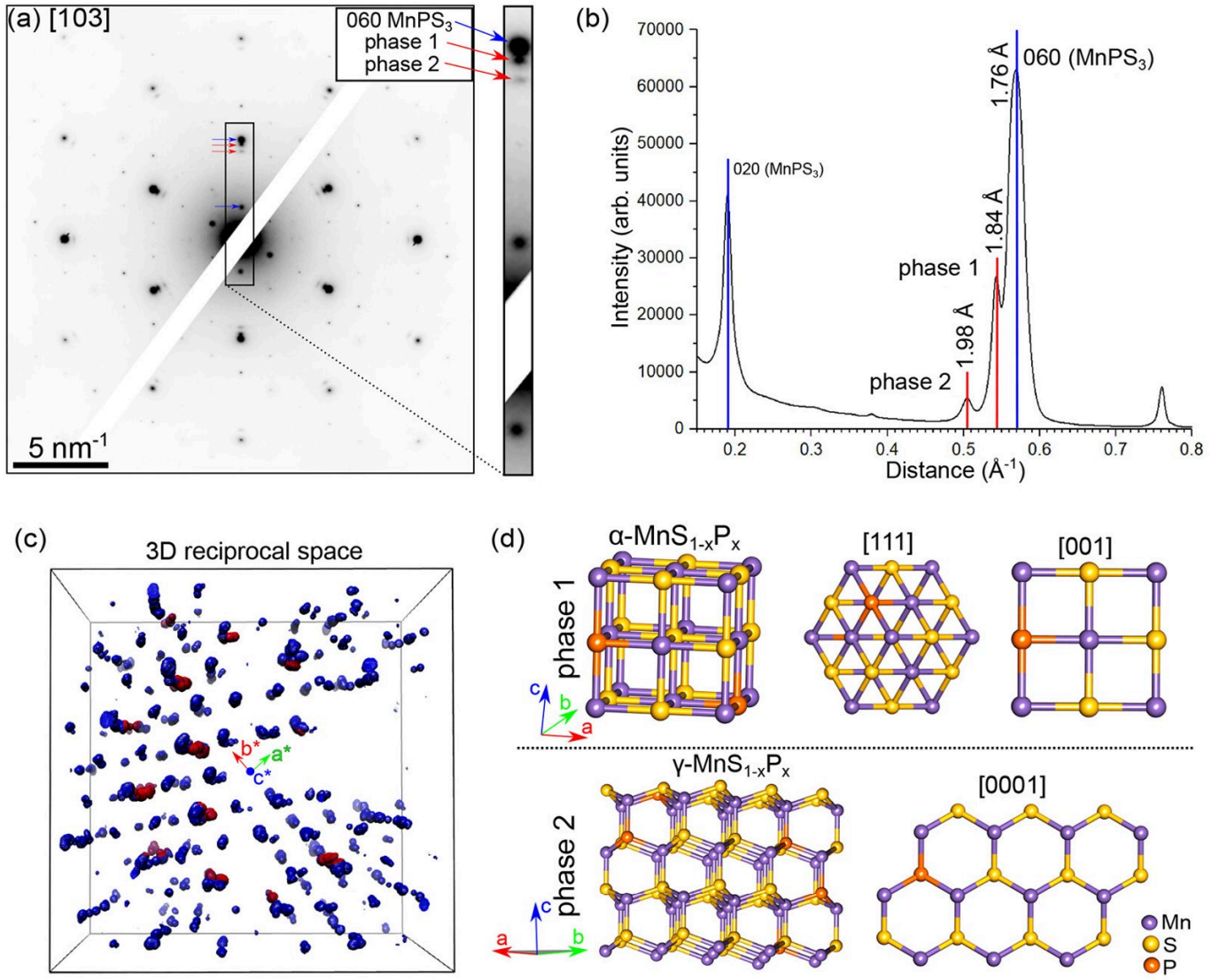

Fig. 3: 3D electron diffraction of the new phases

Annealing in numbers: protocol, contaminants and alabandite

Specimens for annealing were prepared by stamping a PMMA-supported flake onto a microelectromechanical (MEMS) heating chip and removing the polymer in acetone and water. The transition temperature was measured directly in the TEM holder under vacuum (7×10^{-9} bar): the temperature was ramped to 250 °C and then raised stepwise by about 10 °C until the phase transformation occurred, and in a second step to 900 °C in steps of about 50 °C. For the structural investigation the sample was heated to 600 °C for 40 min under vacuum (1×10^{-5} bar) and analyzed afterwards at room temperature. The flakes themselves were obtained by polymer-assisted mechanical exfoliation of bulk crystals, pressed onto a PVA-coated Si substrate and transferred with distilled water to a Quantifoil grid.

The EDX quantification (Brown–Powell model) in Fig. 5b indicates carbon contamination as well as residual oxidized Mn, P and S, and core-loss EELS showed that oxidized phosphorus forms next to the pristine alabandite. In the integrated diffraction pattern of Fig. 5d, an additional peak at 0.45 $Å^{-1}$, corresponding to 2.2 Å, is probably related to graphitic impurities on the surface. The FFT of the HRTEM image (Fig. 5g) gives reciprocal distances of 0.38, 0.54 and 0.77 $Å^{-1}$, in good agreement with the azimuthally integrated pattern. At higher annealing temperatures the polycrys-

talline clusters reassemble into larger alabandite nanocrystals, which are stable as well. The authors concluded that annealing transforms $MnPS_3$ completely into alabandite, with graphitic contamination at the surface and oxidized residuals.

Instruments: HRTEM with a Cs-corrected FEI Titan 80-300 and the Cc/Cs-corrected SALVE microscope (20–80 kV); EDX with a Talos F200X G2 STEM; electron diffraction with the Titan at 300 kV. The EELS energy resolution was 0.6 eV, backgrounds were treated with a power-law model, and crystal thicknesses were obtained from EELS by the log-ratio method.

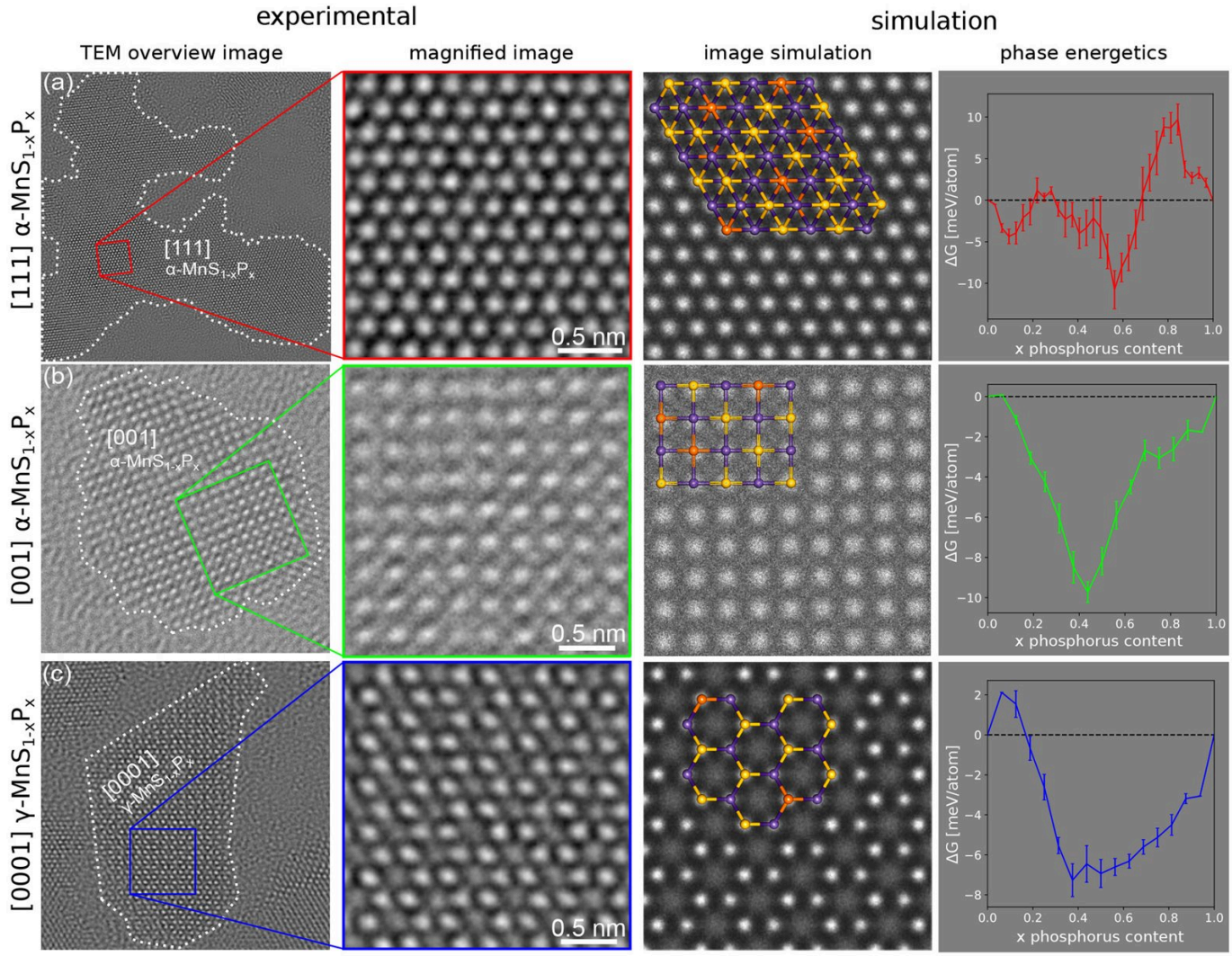

Fig. 4: HRTEM of MnS1−xPx crystals and convex hulls

What are the new MnS polymorphs good for? The researchers investigated their electronic and magnetic properties with DFT calculations and determined the energetically preferred magnetic order for single- and bilayer systems. In the α-MnS phase, the [001] facet is more stable in the antiferromagnetic (AFM) than in the ferromagnetic (FM) state, while the [111] facet prefers to remain ferromagnetic; in the γ-MnS phase, the thickness of the slab changes the order from ferromagnetic to antiferromagnetic. The electronic structure of bulk MnS is significantly changed in the new polymorphs: for the bulk, DFT+U gives a band gap of 1.43 eV between the valence band maximum at the M point and the conduction band minimum at the Γ point, whereas the slabs can be semiconducting or metallic depending on the orientation and thickness of the facets. Because the PBE functional generally underestimates band gaps (see, for example, Ref.[48] and references therein), the team also computed them with DFT+U and the Heyd–Scuseria–Ernzerhof (HSE) hybrid functional; the values, and the effect of phosphorus alloying (Fig. 6), are given in the sixth box.

Band gaps of the MnS facets and the effect of phosphorus

In the monolayer limit, PBE gives band gaps of 0.03 eV for α-[001] MnS and 0.23 eV for γ-[0001] MnS, while the α-[111] monolayer is metallic. DFT+U raises the gaps to 0.83 and 1.98 eV, and HSE gives 0.66 and 2.34 eV, respectively (Table 1 of the paper: bilayers 0.83 and 1.68 eV with DFT+U, 0.66 and 2.04 eV with HSE). The gap of the α-[001] monolayer is indirect, from the valence band maximum at the X point to the conduction band minimum at Γ, whereas the γ-[0001] monolayer has a direct gap at Γ. The γ phase depends strongly on thickness: going from monolayer to bilayer shrinks the gap and turns it from direct to indirect, while the

electronic structure of the α-[001] phase stays almost unchanged. The magnetic moments and ordering do not depend on the degree of localization of the exchange-correlation functional.

To see what phosphorus does, the team computed the projected density of states of the γ-[0001] monolayer, chosen for its relatively large gap, for pristine MnS and for the alloys (Fig. 6). Phosphorus has one electron fewer than sulfur and acts as an acceptor dopant: new occupied states appear at the valence-band edge, the Fermi level shifts towards the valence band, and at higher P concentrations the mixed compound becomes metallic. At 6 % P ($MnS_{0.94}P_{0.06}$) the defect-induced states show a small dispersion formed from the p orbitals of phosphorus and are highly localized on the P atoms, with smaller contributions from the neighbouring Mn atoms; at 25 % P the midgap states are delocalized around the Fermi level.

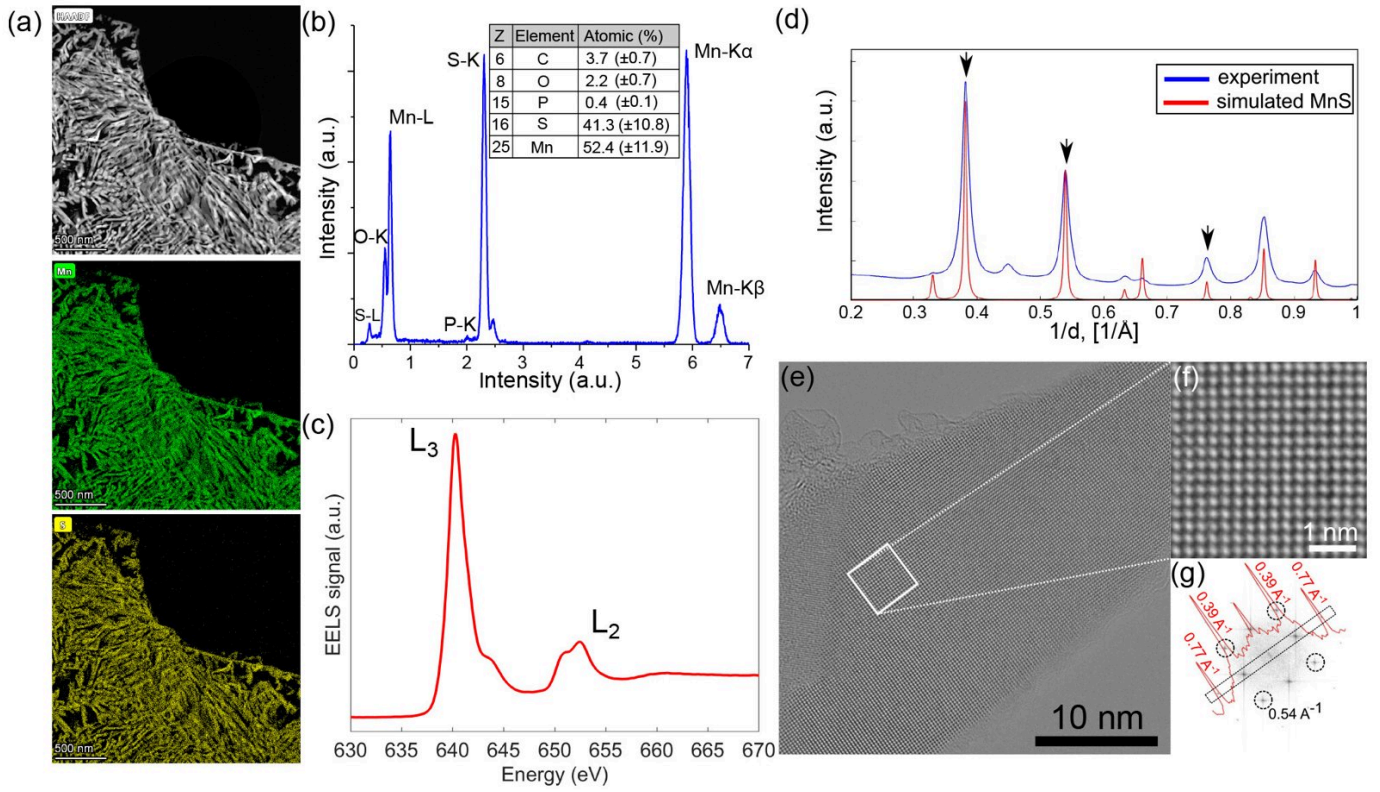

Fig. 5: Analytical TEM of annealed MnPS3

"Our in situ Cc/Cs-corrected HRTEM experiments provided insights into the annealing and electron-beam-induced structure transformations of $MnPS_3$," the authors write. The phase transformations can be controlled locally by the size of the electron beam and by the total electron dose, and mapped on the atomic scale at the same time: suitable dose rates allow the controlled growth of α-MnS-type phases embedded in the host, with the crystals oriented along the direction of the parent $MnPS_3$, while in situ annealing under vacuum converts the whole sample into pure α-MnS. For the MnS structures produced in this way, the ab initio calculations showed that the electronic and magnetic properties depend strongly on the in-plane orientation and the thickness of the crystallites: an α-[001] MnS monolayer is an antiferromagnetic semiconductor with an indirect band gap, a γ-[0001] MnS monolayer a ferromagnetic semiconductor with a direct gap, and the confinement effects in the γ-[0001] facets are strong enough to switch the gap from direct to indirect. Alloying with phosphorus ($MnS_{1-x}P_x$, $0 \le x < 1$) proved to be a powerful way to tailor the electronic and optical properties of the facets, and the mixed phases of both α- and γ-type can be stable for certain phosphorus concentrations.

The broader message of the study is that a few-layer antiferromagnetic host can be transformed on the nanoscale into other stable phases, down to ultrathin films, either wholesale by heat or locally by a focused electron beam, and that the products come with a palette of magnetic and electronic behaviours that depend on how they are cut. "Our electron beam irradiation and annealing experiments show the possibility of a nanoscale transformation of a few-layer antiferromagnetic host into other stable phases, even down to ultrathin films," the authors conclude. The combination of aberration-corrected low-voltage HRTEM, 3D electron diffraction and ab initio theory that made this possible gives a route to writing magnetic and semiconducting MnS patterns into an insulating $MnPS_3$ sheet, one layer at a time.

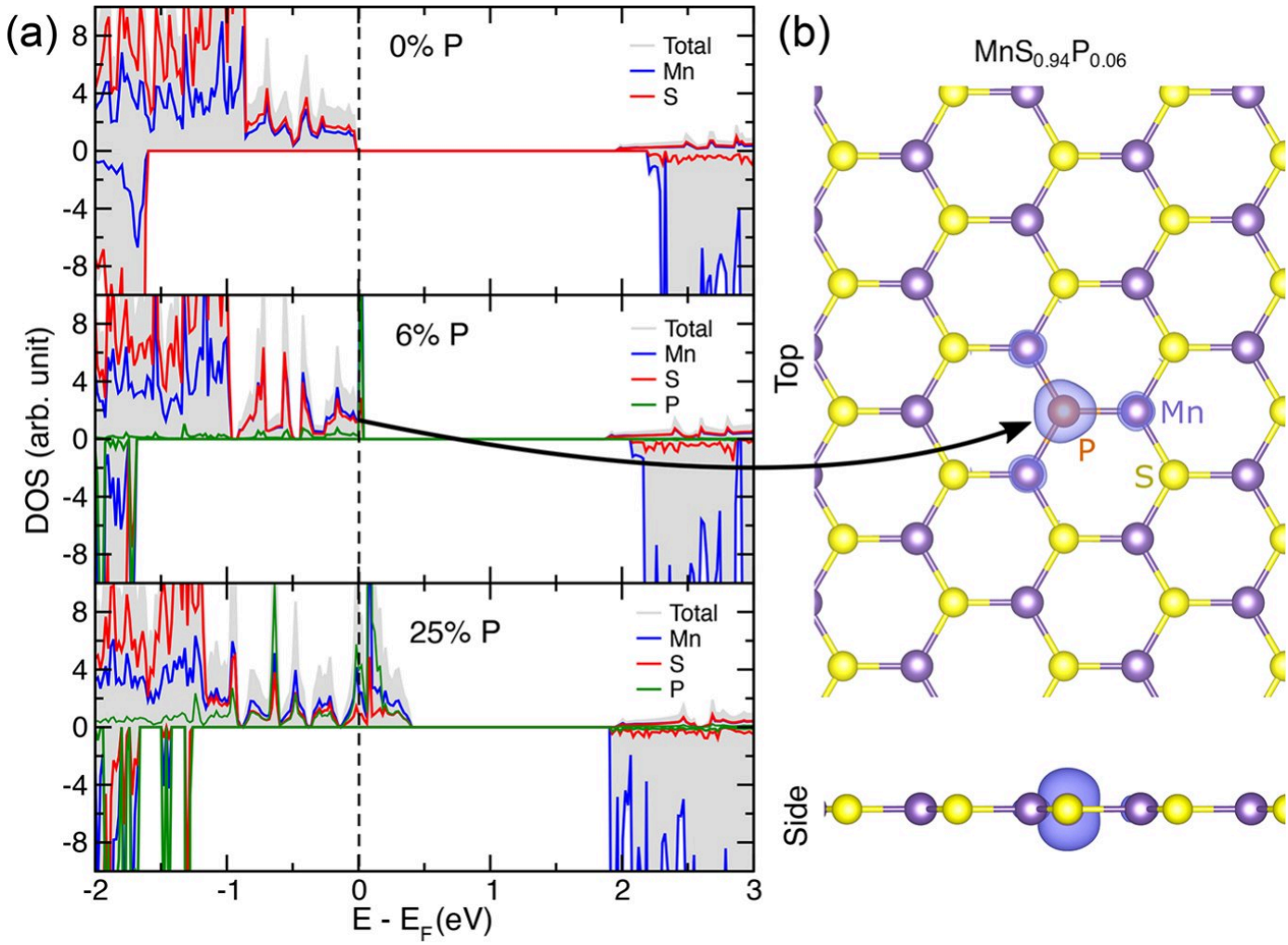

Fig. 6: Phosphorus states in γ-MnS

Resource

Storm, A., Köster, J., Ghorbani-Asl, M., Kretschmer, S., Gorelik, T. E., Kinyanjui, M. K., Krasheninnikov, A. V., Kaiser, U. (2023). Electron-Beam- and Thermal-Annealing-Induced Structural Transformations in Few-Layer $MnPS_3$.

ACS Nano **17**(5), 4250–4260.
https://doi.org/10.1021/acsnano.2c05895

References

1. Novoselov, K., Mishchenko, A., Carvalho, A., & Castro Neto, A. (2016). 2D materials and van der Waals heterostructures. *Science*, **353**, 461. https://doi.org/10.1126/science.aac9439
2. Zhao, X., Kotakoski, J., Meyer, J., Sutter, E., Sutter, P., Krasheninnikov, A., Kaiser, U., & Zhou, W. (2017). Engineering and modifying two-dimensional materials by electron beams. *MRS Bull.*, **42**, 667–676. https://doi.org/10.1557/mrs.2017.184
3. Watanabe, T. (2011). Grain boundary engineering: historical perspective and future prospects. *J Mater Sci*, **46**, 4095–4115. https://doi.org/10.1007/s10853-011-5393-z
4. Zubko, P., Gariglio, S., Gabay, M., Ghosez, P., & Triscone, J. (2011). Interface Physics in Complex Oxide Heterostructures. *Annu. Rev. Condens. Matter Phys.*, **2**, 141–165. https://doi.org/10.1146/annurev-conmatphys-062910-140445
5. Wang, L., Xu, Z., Wang, W., & Bai, X. (2014). Atomic Mechanism of Dynamic Electrochemical Lithiation Processes of MoS_2 Nanosheets. *J. Am. Chem. Soc.*, **136**, 6693–6697. https://doi.org/10.1021/ja501686w
6. Kühne, M., Börrnert, F., Fecher, S., Ghorbani-Asl, M., Biskupek, J., Samuelis, D., Krasheninnikov, A., Kaiser, U., & Smet, J. (2018). Reversible superdense ordering of lithium between two graphene sheets. *Nature*, **564**, 234–239. https://doi.org/10.1038/s41586-018-0754-2
7. Liu, C., Malladi, S., Xu, Q., Chen, J., Tichelaar, F., Zhuge, X., & Zandbergen, H. (2017). In-situ STEM imaging of growth and phase change of individual CuAlX precipitates in Al alloy. *Sci Rep*, **7**, 3–10. https://doi.org/10.1038/s41598-017-02081-9
8. Lehnert, T., Lehtinen, O., Algara–Siller, G., & Kaiser, U. (2017). Electron radiation damage mechanisms in 2D $MoSe_2$. *Applied Physics Letters*, **110**, 033106. https://doi.org/10.1063/1.4973809
9. Susi, T., Meyer, J., & Kotakoski, J. (2017). Manipulating low-dimensional materials down to the level of single atoms with electron irradiation. *Ultramicroscopy*, **180**, 163–172. https://doi.org/10.1016/j.ultramic.2017.03.005
10. Susi, T., Kotakoski, J., Arenal, R., Kurasch, S., Jiang, H., Skakalova, V., Stephan, O., Krasheninnikov, A., Kauppinen, E., Kaiser, U., & Meyer, J. (2012). Atomistic Description of Electron Beam Damage in Nitrogen-Doped Graphene and Single-Walled Carbon Nanotubes. *ACS Nano*, **6**, 8837–8846. https://doi.org/10.1021/nn303944f
11. Meyer, J., Eder, F., Kurasch, S., Skakalova, V., Kotakoski, J., Park, H., Roth, S., Chuvilin, A., Eyhusen, S., Benner, G., Krasheninnikov, A., & Kaiser, U. (2013). Accurate measurement of electron beam induced displacement cross sections for single-layer graphene. *Phys. Rev. Lett.*, **110**, 196102. https://doi.org/10.1103/PhysRevLett.108.196102

12. Wang, Q. H., Bedoya-Pinto, A., Blei, M., Dismukes, A. H., Hamo, A., Jenkins, S., Koperski, M., Liu, Y., Sun, Q.-C., Telford, E. J., Kim, H. H., Augustin, M., Vool, U., Yin, J.-X., Li, L. H., Falin, A., Dean, C. R., Casanova, F., Evans, R. F. L., Chshiev, M., Mishchenko, A., Petrovic, C., He, R., Zhao, L., Tsen, A. W., Gerardot, B. D., Brotons-Gisbert, M., Guguchia, Z., Roy, X., Tongay, S., Wang, Z., Hasan, M. Z., Wrachtrup, J., Yacoby, A., Fert, A., Parkin, S., Novoselov, K. S., Dai, P., Balicas, L., & Santos, E. J. G. (2022). The magnetic genome of two-dimensional van der Waals materials. *ACS Nano*, **16**, 6960–7079. https://doi.org/10.1021/acsnano.1c09150
13. Lin, Y.-C., Björkman, T., Komsa, H.-P., Teng, P.-Y., Yeh, C.-H., Huang, F.-S., Lin, K.-H., Jadczak, J., Huang, Y.-S., Chiu, P.-W., Krasheninnikov, A. V., & Suenaga, K. (2015). Three-fold rotational defects in two-dimensional transition metal dichalcogenides. *Nature Communications*, **6**, 6736. https://doi.org/10.1038/ncomms7736
14. Komsa, H., Kurasch, S., Lehtinen, O., Kaiser, U., & Krasheninnikov, A. (2013). From point to extended defects in two-dimensional MoS_2 : Evolution of atomic structure under electron irradiation. *Phys. Rev. B*, **88**, 035301. https://doi.org/10.1103/physrevb.88.035301
15. Wang, S., Lee, G. D., Lee, S., Yoon, E., & Warner, J. H. (2016). Detailed Atomic Reconstruction of Extended Line Defects in Monolayer MoS_2. *ACS Nano*, **10**, 5419–5430. https://doi.org/10.1021/acsnano.6b01673
16. Lehnert, T., Ghorbani-Asl, M., Köster, J., Lee, Z., Krasheninnikov, A., & Kaiser, U. (2019). Electron-Beam-Driven Structure Evolution of Single-Layer $MoTe_2$ for Quantum Devices. *ACS Appl. Nano Mater.*, **2**, 3262–3270. https://doi.org/10.1021/acsanm.9b00616
17. Meyer, J., Kurasch, S., Park, H., Skakalova, V., Künzel, D., Groß, A., Chuvilin, A., Algara-Siller, G., Roth, S., Iwasaki, T., Starke, U., Smet, J., & Kaiser, U. (2011). Experimental analysis of charge redistribution due to chemical bonding by high-resolution transmission electron microscopy. *Nature Mater*, **10**, 209–215. https://doi.org/10.1038/nmat2941
18. Lin, Y., Dumcenco, D., Huang, Y., & Suenaga, K. (2014). Atomic mechanism of the semiconducting-to-metallic phase transition in single-layered MoS_2. *Nature Nanotech*, **9**, 391–396. https://doi.org/10.1038/nnano.2014.64
19. Sutter, E., Huang, Y., Komsa, H., Ghorbani-Asl, M., Krasheninnikov, A., & Sutter, P. (2016). Electron-Beam Induced Transformations of Layered Tin Dichalcogenides. *Nano Lett.*, **16**, 4410–4416. https://doi.org/10.1021/acs.nanolett.6b01541
20. Lin, Y., Komsa, H., Yeh, C., Björkman, T., Liang, Z., Ho, C., Huang, Y., Chiu, P., Krasheninnikov, A., & Suenaga, K. (2015). Single-Layer ReS_2: Two-Dimensional Semiconductor with Tunable In-Plane Anisotropy. *ACS Nano*, **9**, 11249–11257. https://doi.org/10.1021/acsnano.5b04851
21. Chen, C., Arakawa, K., Lee, J., & Mori, H. (2010). Electron-irradiation-induced phase transformation in alumina. *Scripta Materialia*, **63**, 1013–1016. https://doi.org/10.1016/j.scriptamat.2010.07.028
22. Björkman, T., Kurasch, S., Lehtinen, O., Kotakoski, J., Yazyev, O., Srivastava, A., Skakalova, V., Smet, J., Kaiser, U., & Krasheninnikov, A. (2013). Defects in bilayer silica and graphene: common trends in diverse hexagonal two-dimensional systems. *Sci Rep*, **3**, 3482. https://doi.org/10.1038/srep03482
23. Zhang, Z., Liu, N., Li, L., Su, J., Chen, P., Lu, W., Gao, Y., & Zou, J. (2018). In Situ TEM Observation of Crystal Structure Transformation in InAs Nanowires on Atomic Scale. *Nano Lett.*, **18**, 6597–6603. https://doi.org/10.1021/acs.nanolett.8b03231
24. Zhang, H., Wang, W., Xu, T., Xu, F., & Sun, L. (2020). Phase transformation at controlled locations in nanowires by in situ electron irradiation. *Nano Res.*, **13**, 1912–1919. https://doi.org/10.1007/s12274-020-2711-2
25. Brown, B. (1966). The crystal structures of WTe_2 and high-temperature $MoTe_2$. *Acta Cryst*, **20**, 268–274. https://doi.org/10.1107/s0365110x66000513
26. Cho, S., Kim, S., Kim, J., Zhao, J., Seok, J., Keum, D., Baik, J., Choe, D., Chang, K., Suenaga, K., Kim, S., Lee, Y., & Yang, H. (2015). Phase patterning for ohmic homojunction contact in $MoTe_2$. *Science*, **349**, 625–628. https://doi.org/10.1126/science.aab3175
27. Meng, L., Ma, Y., Si, K., Xu, S., Wang, J., & Gong, Y. (2019). Recent advances of phase engineering in group VI transition metal dichalcogenides. *Tungsten*, **1**, 46–58. https://doi.org/10.1007/s42864-019-00012-x
28. Brec, R. (1986). Review on structural and chemical properties of transition metal phosphorous trisulfides MPS_3. *Solid State Ionics*, **22**, 3–30. https://doi.org/10.1016/0167-2738(86)90055-x
29. Lee, S., Choi, K., Lee, S., Park, B., & Park, J. (2016). Tunneling transport of mono- and few-layers magnetic van der Waals $MnPS_3$. *APL Materials*, **4**, 086108. https://doi.org/10.1063/1.4961211
30. Chittari, B., Park, Y., Lee, D., Han, M., MacDonald, A., Hwang, E., & Jung, J. (2016). Electronic and magnetic properties of single-layer M P X 3 metal phosphorous trichalcogenides. *Phys. Rev. B*, **94**, 184428. https://doi.org/10.1103/physrevb.94.184428
31. Long, G., Henck, H., Gibertini, M., Dumcenco, D., Wang, Z., Taniguchi, T., Watanabe, K., Giannini, E., & Morpurgo, A. F. (2020). Persistence of Magnetism in Atomically Thin $MnPS_3$ Crystals. *Nano Letters*, **20**, 2452–2459. https://doi.org/10.1021/acs.nanolett.9b05165
32. Du, K., Wang, X., Liu, Y., Hu, P., Utama, M., Gan, C., Xiong, Q., & Kloc, C. (2016). Weak Van der Waals Stacking, Wide-Range Band Gap, and Raman Study on Ultrathin Layers of Metal Phosphorus Trichalcogenides. *ACS Nano*, **10**, 1738–1743. https://doi.org/10.1021/acsnano.5b05927
33. Kumar, R., Jenjeti, R., Austeria, M., & Sampath, S. (2019). Bulk and few-layer $MnPS_3$: a new candidate for field effect transistors and UV photodetectors. *J. Mater. Chem. C*, **7**, 324–329. https://doi.org/10.1039/c8tc05011b
34. Glass, D., Jones, J., Shevade, A., & Bugga, R. (2020). Transition Metal Phosphorous Trisulfides as Cathode Materials in High Temperatures Batteries. *J. Electrochem. Soc.*, **167**, 110512. https://doi.org/10.1149/1945-7111/aba0d4
35. Wang, Y., Zhou, Z., Wen, T., Zhou, Y., Li, N., Han, F., Xiao, Y., Chow, P., Sun, J., Pravica, M., Cornelius, A., Yang, W., & Zhao, Y. (2016). Pressure-Driven Cooperative Spin-Crossover, Large-Volume Collapse, and Semiconductor-to-Metal Transition in Manganese(II) Honeycomb Lattices. *J. Am. Chem. Soc.*, **138**, 15751–15757. https://doi.org/10.1021/jacs.6b10225
36. Coradin, T., Coupé, A., & Livage, J. (2003). Intercalation of biomolecules in the $MnPS_3$ layered phase. *J. Mater. Chem.*, **13**, 705–707. https://doi.org/10.1039/b210514d
37. El-Meligi, A., Al-Saie, A., Al-Buflasa, H., & Bououdina, M. (2009). Formation of composite nanomaterial $MnPS_3$ layered structure intercalated with pyridine. *Journal of Alloys and Compounds*, **488**, 284–290. https://doi.org/10.1016/j.jallcom.2009.08.106
38. Veerasubramani, G., Park, M., Choi, J., Lee, Y., Kim, S., & Kim, D. (2019). Rational Combination of an Alabandite MnS Laminated Pyrrhotite Fe1–xS Nanocomposite as a Superior Anode Material for High Performance Sodium-Ion Battery. *ACS Sustainable Chem. Eng.*, **7**, 5921–5930. https://doi.org/10.1021/acssuschemeng.8b05904
39. Chen, X., Li, W., Xu, Y., Zeng, Z., Tian, H., Velayutham, M., Shi, W., Li, W., Wang, C., Reed, D., Khramtsov, V., Li, X., & Liu, X. (2020). Charging activation and desulfurization of MnS unlock the active sites and electrochemical reactivity for Zn-ion batteries. *Nano Energy*, **75**, 104869. https://doi.org/10.1016/j.nanoen.2020.104869
40. Li, N., Zhang, Y., Cheng, R., Wang, J., Li, J., Wang, Z., Sendeku, M., Huang, W., Yao, Y., Wen, Y., & He, J. (2019). Synthesis and Optoelectronic Applications of a Stable p-Type 2D Material: α-MnS. *ACS Nano*, **13**, 12662–12670. https://doi.org/10.1021/acsnano.9b04205
41. Köster, J., Storm, A., Ghorbani-Asl, M., Kretschmer, S., Gorelik, T., Krasheninnikov, A., & Kaiser, U. (2022). Structural and Chemical Modifications of Few-Layer Transition Metal Phosphorous Trisulfides by Electron Irradiation. *J. Phys. Chem. C*, **126**, 15446–15455. https://doi.org/10.1021/acs.jpcc.2c03800
42. Komsa, H., Kotakoski, J., Kurasch, S., Lehtinen, O., Kaiser, U., & Krasheninnikov, A. (2012). Two-Dimensional Transition Metal Dichalcogenides under Electron Irradiation: Defect Production and Doping. *Phys. Rev. Lett.*, **109**, 035503. https://doi.org/10.1103/physrevlett.109.035503
43. Gemmi, M., Mugnaioli, E., Gorelik, T., Kolb, U., Palatinus, L., Boullay, P., Hovmöller, S., & Abrahams, J. (2019). 3D Electron Diffraction: The Nanocrystallography Revolution. *ACS Cent. Sci.*, **5**, 1315–1329. https://doi.org/10.1021/acscentsci.9b00394

44. Sombuthawee, C., Bonsall, S. B., & Hummel, F. A. (1978). Phase equilibria in the systems ZnS–MnS, ZnS–$CuInS_2$, and MnS–$CuInS_2$. *Journal of Solid State Chemistry*, **25**, 391–399. https://doi.org/10.1016/0022-4596(78)90125-1

45. Clendenen, R. L., & Drickamer, H. G. (1966). Lattice Parameters of Nine Oxides and Sulfides as a Function of Pressure. *The Journal of Chemical Physics*, **44**, 4223–4228. https://doi.org/10.1063/1.1726610

46. Prince, A. (1966). Alloy Phase Equilibria. Elsevier, Amsterdam.

47. Tan, H., Verbeeck, J., Abakumov, A., & Van Tendeloo, G. (2012). Oxidation state and chemical shift investigation in transition metal oxides by EELS. *Ultramicroscopy*, **116**, 24–33. https://doi.org/10.1016/j.ultramic.2012.03.002

48. Yang, Z., Peng, H., Sun, J., & Perdew, J. (2016). More realistic band gaps from meta-generalized gradient approximations: Only in a generalized Kohn-Sham scheme. *Phys. Rev. B*, **93**, 205205. https://doi.org/10.1103/physrevb.93.205205